Multi-pronged Atomistic Simulations

Thermo-physical and Diffusional Properties of Uranium-Neptunium and Thorium-Neptunium Mixed Oxides

P.S. Ghosh and A.K. Arya*

Glass and Advanced Materials Division

Bhabha Atomic Research Centre, Mumbai-400085, India

ABSTRACT

Burn-up of $(U,Pu)O_2$ mixed oxide (MOX) fuels generate additional long-lived minor actinides (MAs) in the yield range 0.1-1.0%. The Np and other MAs are a major concern for the storage of spent fuels due to their long-term radiotoxicity and heat generation in the spent fuel. The burn-up of ThO_2-based MOX generates $(Th,U,MA)O_2$ and/or $(Th,Pu,MA)O_2$ MOX which may alter the thermal properties of the fuel. Experimental determination of thermo-physical and diffusional properties of these MOX is difficult due to their radio-toxicity. A multi-pronged atomistic simulation approach consisting of (a) first-principles density functional theory for evaluation of ground state stability, complex magnetic interactions, defect formation energies and elastic properties, (b) Monte-Carlo based approach to exactly model disordered alloys and (c) molecular dynamics calculations for evaluation of diffusional and thermal properties of $U_{1-x}Np_xO_2$ and $Th_{1-x}Np_xO_2$ MOX has been employed. The generation of thermo-physical and diffusional properties database of Np-containing MOX will help design and fabrication of new fuels and perform safety analysis.

Keywords: Thermo-physical parameters, Diffusion, MOX fuel, Atomistic simulations, DFT, Monte-Carlo.

Introduction

Neptunium (^{237}Np, half life = 2.14 x 10^6 years), is formed in nuclear fuels as a byproduct, either by α decay of ^{241}Am or by the (n,γ) reaction of ^{235}U followed by β emission. In reactors utilizing $U_{1-x}Pu_xO_2$ mixed oxides (MOX) fuel; NpO_{2-x} is generated predominantly along with other minor actinides (MA's) (with a yield of 0.1-1.0%) and gets accumulated due to its long half-life. Moreover, it is an important nuclide for geological disposal of spent fuel generated from open fuel cycle reactor operation, where the spent fuel is stored for the long term. For reactors operating in a closed fuel-cycle mode, spent fuels are reprocessed chemically to isolate MA's, which are reused for energy production in fast reactors as $U_{1-x-y}Pu_xMA_yO_2$ MOX. As a result, MA's can be transmuted into less radiotoxic and lighter isotopes, which reduce the long-term radiotoxic impact of these materials. The transmutation of MA's in fast reactors can be performed in homogeneous (2-6 wt.% MAs, homogeneously added to fuel) and heterogeneous modes (10-30 wt.% MAs is added to transmutation targets) [1-5]. Additionally, ThO_2 based MOX ($Th_{1-x}U_xO_2$ and $Th_{1-x}Pu_xO_2$) has emerged as an alternate high performance fuel with additional advantages of lower radiotoxic nuclear waste generation and easy management and storage of long-lived highly radioactive nuclides, compared to conventional UO_2 based MOX [1-14]. $Th_{1-x}MA_xO_2$ MOX can be formed in a nuclear reactor from the transmutations of $Th_{1-x}U_xO_2$ and $Th_{1-x}Pu_xO_2$ MOX. Hence, a better understanding of $U_{1-x}Np_xO_2$ and $Th_{1-x}Np_xO_2$ pseudo-binary phase diagrams, including thermodynamic and electronic properties, is highly desirable in order to assess the phase stability of these materials.

Under irradiation, a large number of point defects are produced and many of these point defects recombine instantly during the cascade processes at elevated temperature [15]. In MOX fuels, the production and migration of oxygen vacancies and interstitials are of primary interest because their mobility plays an important role in the micro-structural evolution and the diffusion-controlled formation of defect clusters, bubbles, dislocation loops, and the restructuring of fuels [15-17]. Therefore, it is important to increase our understanding of thermal and diffusional properties of MAO_2, $(U,Pu,MA)O_2$ and $(Th,U,Pu,MA)O_2$ MOXs at high temperatures. This will contribute to better transmutation fuel fabrication and to the prediction of fuel behavior under irradiation and thus leads to improve fuel performance. In this regard, NpO_2 based MOX, is specifically important because of its high yield during the burn-up of fuels. The effect of the addition of MAs in MOX on thermal and diffusional properties has been studied relatively rarely by experimental means because of the radio-toxicity involved in these materials. Even though, the experiments were performed it was limited to specific compositions of MAO_2 and temperature ranges over which the properties were measured. The evaluation of thermal and diffusional properties using atomistic simulations can provide fundamental insights at a level not achievable through experiment alone [7-19]. Present study adopts quantum and classical mechanical based simulation strategies to determine thermodynamical, thermo-physical and diffusional properties of $U_{1-x}Np_xO_2$ and $Th_{1-x}Np_xO_2$ MOX. Firstly, ground state formation enthalpies of $U_{1-x}Np_xO_2$ and $Th_{1-x}Np_xO_2$ MOX accounting for their magnetic configurations are calculated using density functional theory (DFT) based simulations. Further, electronic structures and elastic properties of pure oxides and MOX are calculated. The special quasi-random structures (SQS) approach and *U*-ramping method are used to overcome difficulties related to the modeling of random alloys and to achieve the correct ground state, respectively. Secondly, the thermal expansion, thermal conductivity and diffusion properties of $U_{1-x}Np_xO_2$ and $Th_{1-x}Np_xO_2$ MOX are studied in the 300-2000 K temperature range using static and molecular

dynamical (MD) simulations with classical empirical potentials as a first step towards the investigation of more complex $(U,Pu,Np)O_2$ and $(Th,U,Pu,Np)O_2$ MOX fuels.

2. Computational Methodology

In order to calculate the formation energies and the electronic structures of $U_{1-x}Np_xO_2$ and $Th_{1-x}Np_xO_2$ MOX, *ab initio* total energy calculations are carried out using spin polarised mode of density functional theory (DFT) as implemented in the VASP package. The standard projected augmented wave (PAW) potentials and a plane-wave basis set with a cut off value of 500 eV were used in all cases. The exchange-correlation term was modelled using the generalized gradient approximation (GGA), parameterized by Perdew, Burke and Ernzerhof (PBE). To describe the behaviour of the localised *f* states in Th, U and Np, we included the orbital-dependent Coulomb potential (Hubbard *U*) and the exchange parameter *J*, as formulated by Liechtenstein *et al.* In our calculations *U*=4.5 and *J* =0.5 eV was used as suggested by Kotani *et al.* based on their X-ray photoemission spectroscopic (XPS) analysis of UO_2. The DFT+*U* calculation method for a magnetic system can lead to several metastable configurations for self-consistent-field solutions. The *U*-ramping method was used in this study to determine electron orbital occupation corresponding to the correct ground state of magnetic system as proposed by Mereding *et al.*. In order to determine the true magnetic ground states of UO_2 and NpO_2, the relativistic spin-orbit interactions (SOI) were also considered in our calculations. In order to study phase stability of $U_{1-x}Np_xO_2$ and $Th_{1-x}Np_xO_2$ MOX, 96 atom special quasirandom structures (SQS) were used. A 4×4×4, 8x8x4 and 8×8×8 *k* point mesh were used in all calculations of structural optimization for 96, 24 and 12 atoms cells, respectively [17].

The MD simulations to determine thermal properties were carried out using the Large-scale Atomic Molecular Massively Parallel Simulator (LAMMPS) where the Coulombic interactions were calculated using the Ewald method. The empirical interatomic potential model used in this study combines a pair-wise (Buckingham-Morse type) with a many body interaction term. This particular potential model was developed to reproduce experimental thermo-mechanical properties of actinide oxides AcO_2 with An={Ce, Th, U, Np, Pu, Am, Cm} in a temperature range of 300 K to 3000 K and to reproduce the Cauchy violation in the elastic properties. This potential model was later extended to include potential parameters for the MOX compositions of AcO_2. In the present study, the MD supercell was constructed from 4000 cations and 8000 anions in an array of 10x10x10 unit cells for $U_{1-x}Np_xO_2$ and $Th_{1-x}Np_xO_2$ and their end members. MD runs were performed with a 1 fs time step over the temperature range 300 K to 3000 K at interval of 25 K, with the NPT ensemble at zero external pressure using the Nosé-Hoover thermostat and barostat with a time constant of 0.1 ps and 0.1 ps, respectively. Each simulation of thermodynamical quantities was carried out initially for 40 ps to establish equilibration (at the desired temperature) and then for another 10 ps to obtain average values of the thermodynamic quantities while heating the system. For calculations of thermal conductivity within LAMMPS, the Green-Kubo (GK) formalism was adopted where an estimate of the transport coefficient relies on the integral of an accurate time-correlation of the equilibrium fluctuations of heat flux in the system [16].

The binding energies and migration barriers were calculated using static calculations in a 10x10x10 supercell. The calculations were performed to determine binding energies of configurations

where the oxygen vacancy is first (1st NN) or second (2nd NN) nearest neighbor (NN) with respect to the dopant atom. The calculations of migration barrier were performed using the nudged elastic band method as implemented in LAMMPS code in static condition. The migration barriers were calculated for the hopping of oxygen vacancy to a NN site along the <001> direction, which is known to be the lowest barrier migration direction in fluorite-based oxides. In order to determine the diffusion of the oxygen vacancy mean square displacements (MSD) were calculated for 5 ns for a temperature range from 750 K to 2000 K. To capture substantial oxygen diffusion on the limited MD timescale, 1% oxygen vacancies in the supercell was introduced. The charge imbalance in the system was compensated by an equivalent background charge [16].

3. Results and Discussions

a) Formation enthalpies of MOX

The variation of structural and electronic properties of UO_2 and NpO_2 with collinear ferromagnetic (FM), collinear anti-ferromagnetic (AFM) and non-collinear AFM arrangements of the uranium and neptunium magnetic moments are investigated while ramping up the U_{eff} from 0 eV, corresponding to standard density functional theory, upto U_{eff} = 4 eV, the value that correctly reproduces the AFM ground state of bulk UO_2 and NpO_2 (the so-called U_{eff}-ramping method). Analysis of structural and electronic properties of UO_2, NpO_2 and ThO_2 shows that spin-orbit interactions (SOI) had only a small effect on lattice parameters and electronic properties. The effect of FM and collinear AFM ordering is considered in determining the mixing enthalpies (ΔH_{mix}) [17].

Fig.1(a) shows ΔH_{mix} calculated using SQS in FM and ordered AFM configurations (along [001] direction) of $Th_{1-x}Np_xO_2$ MOX as a function of composition (x). The FM-SQS results (circles) are generated using the FM ground state of NpO_2, while AFM results (triangles) are generated using the AFM ground state of NpO_2. The calculated ΔH_{mix} values are positive and nearly symmetric around x = 0.5, suggesting a miscibility-gap phase diagram for fluorite structured random solid solutions, consistent with previous calculations. The ΔH_{mix} of the AFM configuration is higher compared to the FM configuration maximum by 0.19 kJ/mole. A quadratic fit of the ΔH_{mix} (shown as a dashed curve in Fig.1(a)) approximates $Th_{1-x}Np_xO_2$ MOX system as a regular solid solution. The interaction parameter Ω can be obtained from the formula:

$$\Omega = \frac{\Delta H_{mix}}{X(1-x)} \quad \text{(1)}$$

and results are Ω = 2.82 and 3.47 kJ/mole for SQS-FM and AFM configuration, respectively. Our DFT calculated endothermic interaction parameters are lower compared to experimental value of 15.1±2.2 kJ/mol for ThO_2-CeO_2 MOX. Although, a lower value (for $Th_{1-x}Np_xO_2$) is expected compared to $Th_{1-x}Ce_xO_2$ considering lower mismatch of ionic radii for ThO_2-NpO_2 (Th^{+4}=1.19 Å, Np^{+4}=1.12 Å, 8-fold coordination) compared to ThO_2-CeO_2 (Th^{+4}=1.19 Å, Ce^{+4}=1.11 Å, 8-fold coordination). The difference in experimental and theoretical results of ΔH_{mix} can also be attributed to vibrational contribution to ΔH_{mix} and degree of configurational disorder present in the solid solutions. The vibrational contribution is expected to be negligibly small at room temperature. In our calculation random configurational disorder is assumed and thus neglecting any contributions from short-range order (SRO) which may be present in the experimental solid solutions that are equilibrated at high temperature.
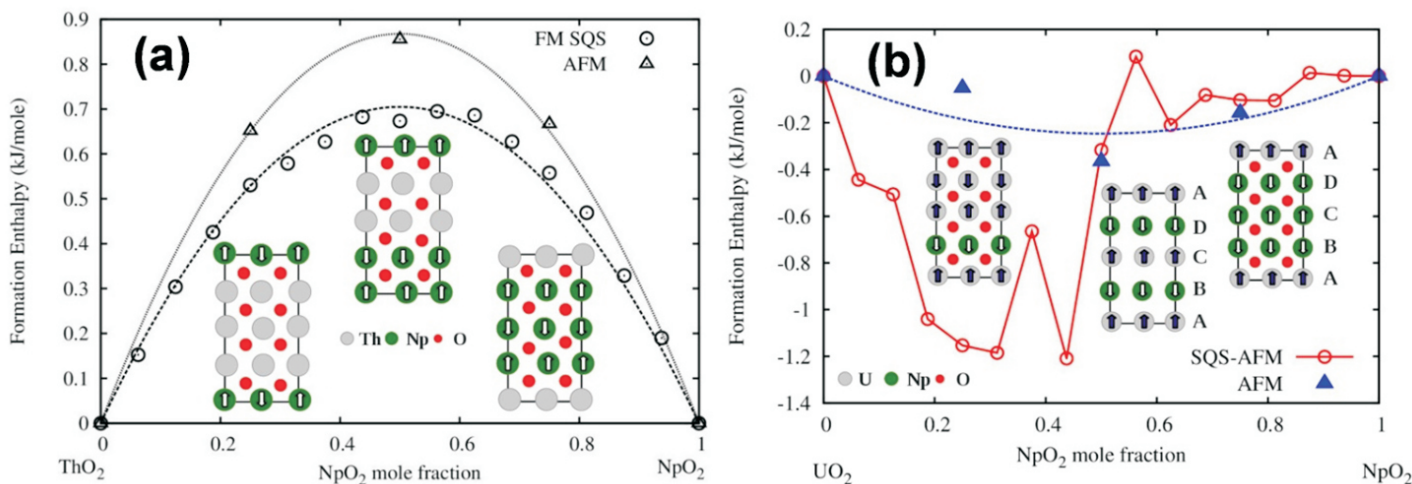
Fig.1: GGA+*U* calculated formation enthalpies of (a) Th$_{1-x}$Np$_x$O$_2$ MOX in FM (open circles) and AFM (open triangles) configurations. Similarly, formation enthalpies of (b) U$_{1-x}$Np$_x$O$_2$ MOX in random AFM (open circles) and ordered AFM (solid triangles) along [001] configurations. The magnetic structures of Th$_{1-x}$Np$_x$O$_2$/U$_{1-x}$Np$_x$O$_2$ (x=0.25, 0.50, 0.75) MOX in AFM configurations is shown with small arrows on atoms.

Fig.1(b) shows formation enthalpies of random AFM solid solutions calculated employing SQS and AFM configurations ordered along [001] direction of U$_{1-x}$Np$_x$O$_2$ MOX. The AFM SQS results (circles) are generated using the AFM ground state of UO$_2$ and NpO$_2$ with the spins of Np and U atoms distributed in such a fashion that the overall spin is zero or a minimum. Because neptunium and uranium atoms have different local spins, 3 μ_B/Np^{4+} ion and 2 μ_B/U^{4+} ion, the total magnetic moment is not zero for U$_{1-x}$Np$_x$O$_2$ MOX in their ordered AFM states (for x ≠ 0 and 1). For U$_{0.75}$Np$_{0.25}$O$_2$, U$_{0.50}$Np$_{0.50}$O$_2$ and U$_{0.25}$Np$_{0.75}$O$_2$ MOX, the effective magnetic moments are 1.92 μ_B, 11.84 μ_B and 5.95 μ_B, respectively. The ΔH_{mix} of ordered AFM and SQS AFM configurations are negative or very close to zero. For SQS AFM configurations ΔH_{mix} are negative up to U$_{0.50}$Np$_{0.50}$O$_2$ with maximum value of -1.21 kJ/mole at U$_{0.4375}$Np$_{0.5625}$O$_2$ while Np-rich U$_{1-x}$Np$_x$O$_2$ MOX has ΔH_{mix} values close to zero (< - 0.2 kJ/mol). The ΔH_{mix} versus concentration curve is not smooth showing small jumps at some specific compositions, which may be due to the slightly higher mismatch of correlation functions of generated SQS structures at these compositions with those of their ideal-random alloy counterparts. The fitting of equation (1) to our DFT calculated ΔH_{mix} values for AFM configurations (shown by dashed line in Figure 1(b)) gives Ω = -0.985 kJ/mole. High temperature oxide melt solution calorimetry measured ΔH_{mix} values are zero within experimental error bar for Th$_{1-x}$U$_x$O$_2$ and U$_{1-x}$Ce$_x$O$_2$ MOX systems. The negative values of Hmix in the U-rich U$_{1-x}$Np$_x$O$_2$ MOX is corroborating with the fact that long range AFM ordering is present in single crystal U$_{0.75}$Np$_{0.25}$O$_2$ below T$_N$ = 17 K.

b) Thermal Expansion

Fig.2 (a) shows the increase of lattice parameter as a function of temperature for Th$_{1-x}$Np$_x$O$_2$ (x=0, 0.065, 0.125, 0.25, 0.50, 0.75 and 1.00) and U$_{1-x}$Np$_x$O$_2$ (x= 0, 0.065, 0.125, 0.3125, 0.50, 0.6875 and 1.0). High temperature XRD data for ThO$_2$, UO$_2$ and NpO$_2$ are also included in the figure. The overall decrease in lattice parameters compares well with experimental data, which follow Vegard's law. This is demonstrated by fitting our MD calculated lattice parameters to a straight line equation: a(U$_{1-x}$Np$_x$O$_2$) = 5.4699 – 0.0359 x, 1 < x < 0, since it matches well with Vegard's law of the form a(U$_{1-x}$Np$_x$O$_2$) = 5.4702 – 0.0364 x, 1 < x < 0, fitted to the experimental lattice parameters of UO$_2$ and NpO$_2$ (5.4702 Å and 5.4338Å, respectively). Thermal expansion coefficients (α) (in 300-1300 K range) are

11.12, 11.08, 11.00, 10.85, 10.77, 10.65, 10.35 K^{-1} for x= 0, 0.065, 0.125, 0.3125, 0.50, 0.6875 and 1.0 in U$_{1-x}$Np$_x$O$_2$, respectively. These values are in good agreement with experimental values of 10.34, 10.20, 10.18, 10.08 and 10.01 K^{-1} for x= 0.0, 0.1, 0.5, 0.7, and 1.0, respectively. For ThO$_2$, values for a_{300} and α match previous high-temperature XRD data with only a 2% deviation. Nevertheless, the calculated value of UO$_2$ and NpO$_2$ are over predicted by 7.6% and 3.4%, respectively, compared to experimental values. The values of a_{300} for Th$_{1-x}$Np$_x$O$_2$ decrease with increasing NpO$_2$ concentration and the overall decrease in lattice parameters can be represented as: a(Th$_{1-x}$Np$_x$O$_2$) = 5.59538 - 0.162021 x, 1 < x < 0. It matches well with Vegard's law of the form a(Th$_{1-x}$Np$_x$O$_2$) = 5.5967 – 0.0534 x, 1 < x < 0, fitted to the experimental lattice parameters of ThO$_2$ and NpO$_2$ (5.5967 Å and 5.4338 Å, respectively). The variation of lattice parameters of Th$_{1-x}$Np$_x$O$_2$ and U$_{1-x}$Np$_x$O$_2$ MOX with the variation of NpO$_2$ content, x, is shown in **Fig.2(b)**. Accompanying the increment of temperature, from 300 K to 2000 K, the structural parameters of both Th$_{1-x}$NpxO$_2$ and U$_{1-x}$Np$_x$O$_2$ decrease linearly with increasing value of x. From comparison of the two figures, we can clearly see that the reduction rate of Th$_{1-x}$Np$_x$O$_2$ is greater than U$_{1-x}$Np$_x$O$_2$ MOX, which indicates that the NpO$_2$ has a far greater influence on lattice parameters for Th$_{1-x}$Np$_x$O$_2$ than U$_{1-x}$Np$_x$O$_2$ MOX at same value of x. This phenomenon can be explained by the differences in ionic size of Th^{4+} (1.19 A), U^{4+} (1.14 A) and Np^{4+} (1.12 Å) in 8-fold coordination. Further, the variation of lattice parameters (in Å) of Th$_{1-x}$Np$_x$O$_2$ and U$_{1-x}$Np$_x$O$_2$ MOX can be presented as a function of NpO$_2$ concentration (x, 1.0 ≥ x ≥ 0.0) and temperature (T, 2000 ≥ T ≥ 300):

$$a(Th_{1-x}Np_xO_2) = -0.160777(x) + 4.44721 \times 10^{-5}T + 6.87589 \times 10^{-9}T^2 + 5.57487$$

$$a(U_{1-x}Np_xO_2) = -0.0397186(x) + 4.56747 \times 10^{-5}T + 8.35801 \times 10^{-9}T^2 + 5.45702$$

(2)

c) Thermal Conductivity

Fig.2(c) compares calculated thermal conductivity (TC) of Th$_{1-x}$Np$_x$O$_2$ (x=0.0, 0.0625 and 0.125) as a function of temperature with experimental values for pure ThO$_2$ [6-8]. Fig.2(d) compares calculated TC of U$_{1-x}$Np$_x$O$_2$(x=0.0, 0.0625, 0.125, 0.5 and 1.0) as a function of temperature, with experimental values for end members UO$_2$, NpO$_2$ and U$_{0.5}$Np$_{0.5}$O$_2$. The TC values of UO$_2$ and NpO$_2$ are quite close across this temperature range. However, classical MD
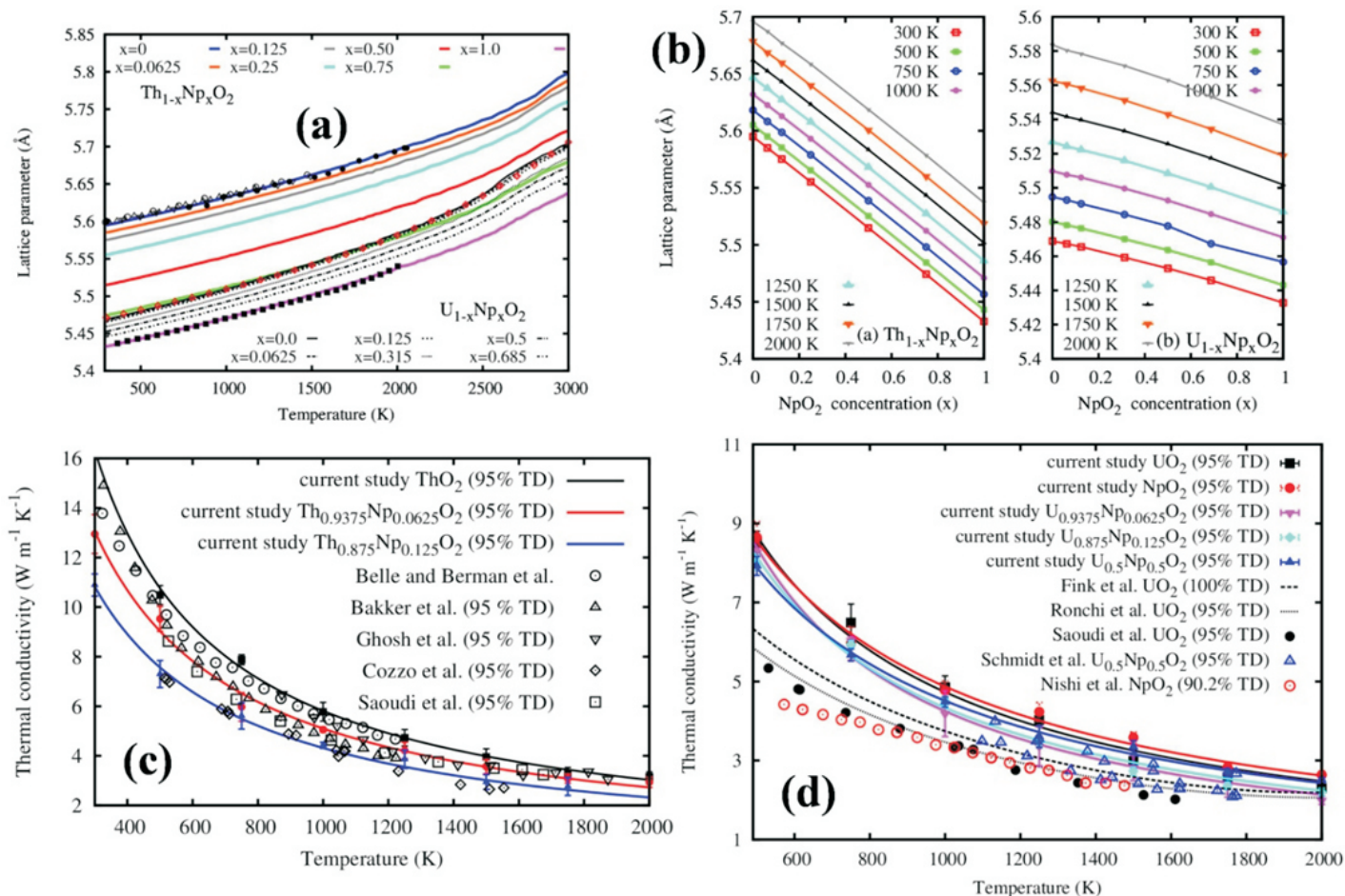
Fig.2: (a) The variation of calculated lattice parameters for $Th_{1-x}Np_xO_2$ (x=0.0, 0.0625, 0.125, 0.25, 0.50, 0.75 and 1.0) and $U_{1-x}Np_xO_2$ (x=0.0, 0.0625, 0.125, 0.3125, 0.5, 0.6875 and 1.0) as a function of temperature up to 3000 K. Lines present calculated values and points present high temperature XRD values of ThO_2, UO_2 and NpO_2. (b) Lattice constants calculated by MD simulations as a function of NpO_2 concentration (x) for $Th_{1-x}Np_xO_2$ and $U_{1-x}Np_xO_2$ solid solution. MD calculated thermal conductivity values (at 95% TD) for (c) $Th_{1-x}NpxO_2$ (x=0.0, 0.0625 and 0.125) and (d) $U_{1-x}Np_xO_2$ (x=0.0, 0.0625, 0.125, 0.5 and 1.0) are shown as a function of temperature. Experimental values of ThO_2, UO_2, NpO_2, and $(Np0.5U0.5)O_2$ MOX are compared with the calculated values.

calculated TC values of both UO_2 and NpO_2 are grossly overestimated at lower temperature (< 1000 K) compared to experimental values. In order to improve the accuracy of the thermal-conductivity predictions for UO_2, MD results need be corrected for the spin-phonon-scattering mechanism by adding the corresponding relaxation time derived from existing experimental data as shown by Liu *et al.*.

Fig.2(d) also indicates a small reduction in TC values for $U_{1-x}Np_xO_2$, even at low temperatures, due to reduction in the phonon mean free path coming from scattering associated with a non-uniform cation sublattice. The degradation of the UO_2 thermal conductivity due to Np substitutional defects is relatively small compared to the addition of Np in ThO_2. The calculated TC values of $(Np_{0.5}U_{0.5})O_2$ are lower than those of pure UO_2 and NpO_2 due to higher impurity-phonon scattering at low temperatures (<750 K). The calculated TC values of $(Np_{0.5}U_{0.5})O_2$ also match the experiment well throughout the temperature range with maximum deviation of 15%. This is consistent with the experimental observation that the TC of NpO_2 with 95%TD was close to that of $(Np_{0.5}U_{0.5})O_2$ above 1098 K. At higher temperatures (above 750 K), the TC values are almost independent of the NpO_2 concentration and the TC values for UO_2, NpO_2 and $(U,Np)O_2$ MOX almost superimpose at high temperatures [16].

Table 1. A comparison of constants A and B of the equations $1/k = A+BT$ for $Th_{1-x}Np_xO_2$ (x=0.0, 0.0625 and 0.125) and $U_{1-x}Np_xO_2$ (x=0.0, 0.0625, 0.125, 0.5 and 1.0) derived from MD simulations and from experimental measurements. The C_{PQ} values are also shown in the table.

	A($\times10^{-2}$)mKW^{-1}	B($\times10^{-4}$)mW^{-1}
ThO$_2$		
MD, this study	1.282	1.466
Experiment [7]	4.200	2.250
Experiment [6]	1.000	2.300
Experiment [8]	3.170	1.699
(Th$_{0.9375}$Np$_{0.0625}$)O$_2$ MD, this study	2.356	1.581
(Th$_{0.875}$Np$_{0.125}$)O$_2$ MD, this study	3.034	1.543
UO$_2$		
MD, this study	1.896	1.923
Experiment [6]	6.548	2.353
Experiment [6]	6.240	2.399
(Th$_{0.9375}$Np$_{0.0625}$)O$_2$ MD, this study	2.981	2.32
(Th$_{0.875}$Np$_{0.125}$)O$_2$ MD, this study	3.045	2.16
(U$_{0.5}$Np$_{0.5}$)O$_2$ MD, this study	3.213	1.89
NpO$_2$		
MD, this study	2.861	1.770
Experiment (573-1473K)[29]	9.447	1.797
C_{Th-Np}= 4.198x10^{-1}		
C_{U-Np}= 6.674 x 10^{-3}		

The calculated TC values of MOX are fitted to the relation of phonon conduction as proposed by Adachi *et al.*:

$$k=1/[xW_{PO2}+(1-x)W_{QO2}+x(1-x)C_{PQ}], \qquad (3)$$

where x = fractional concentration of lattice defects in $P_xQ_{1-x}O_2$, and $W_{PO2}=A_{PO2}+B_{PO2}T$ and $W_{QO2}=A_{QO2}+B_{QO2}T$ are thermal resistivity of end-members. If $x = 0$ or $x = 1$, the above equation becomes

$$k=1/(A+BT) \qquad (4)$$

The 'A' and 'B' represent defect-phonon scattering and phonon-phonon scattering contributions, respectively. The C_{PQ} arises due to the random distribution of P and Q atoms on a given sublattice. The influence of substituted impurities on the TC is attributed to an increase in parameter 'A' which is temperature independent. This results from interactions of phonons with lattice imperfections, impurities, isotopic, or other mass differences as well as defects such as grain boundaries and dislocations in the sample. Parameter 'B' can be considered a constant and the second term, namely $B.T$, represents the intrinsic lattice thermal resistivity caused by phonon-phonon scattering. With increasing temperature this term becomes dominant. One pair of A and B constants can be obtained for each solid solution composition by polynomial fitting of the thermal resistivity versus temperature data (Table 1). Moreover, MD calculated values are also fitted to above equation to determine the parameter C_{PQ} also shown in Table 1.

d) Oxygen Diffusion

The NEB calculated oxygen vacancy migration energies (E_m) for ThO_2, UO_2 and NpO_2 are reported in Table 2. The E_m of ThO_2 is highest and E_m's of UO_2 and NpO_2 differ by only 0.018 eV. Grovers *et al.* [34] calculated the E_m of UO_2 using nineteen different interatomic potentials and found that E_m's lie between 0.3 and 0.5 eV. The NEB calculated e_m of 0.40 eV, obtained from the current potential, is in good agreement with those calculated earlier using different potentials as shown in the Table 2. Behera *et al.* calculated E_m for ThO_2 using eight different interatomic potentials and found that E_m's lie between 0.52 and 0.79 eV. Our NEB calculated E_m of 0.54 eV is within this range. Finally, Aidhy *et al.* calculated E_m for UO_2, ThO_2 and NpO_2 and found very similar values, as shown in Table 2.

Table 2 also reports the energy gained or lost when an oxygen vacancy occupies a site close to a single dopant in an otherwise dopant free supercell. The binding energy of the oxygen vacancy to the dopant atom, and is defined as $E_b = E(NN) − E(infinite)$, where $E(NN)$, is the energies of the supercell in which the oxygen vacancy occupies a near neighbor (1st NN) and second near neighbor (2nd NN) site with respect to the dopant atom and $E(infinite)$ is the energy of the supercell with only a dopant or only an oxygen vacancy is infinitely separated. These configurations are then used to identify the migration activation energies for an oxygen ion moving to the vacant site adjacent to the dopant cation. The presence of the dopant results in either small increase or decrease in activation energy depending on the ionic radius of the cations (Table 2).

In order to determine oxygen diffusivity in $Th_{1-x}Np_xO_2$ and $U_{1-x}Np_xO_2$ MOX, we compare the mean square deviations (MSD) of pure ThO_2, UO_2, NpO_2 and $Th_{1-x}Np_xO_2$, $U_{1-x}Np_xO_2$ MOX at five intermediate compositions calculated at 750 K, as shown in Fig.3 (a) and (b). We find that NpO_2 has a higher MSD slope than ThO_2, which can be attributed to the higher E_m of ThO_2 compared to any other oxide studied here (Table 2). Fig.3(a) also shows that the MSD slope

of $Th_{0.125}Np_{0.875}O_2$ and $Th_{0.25}Np_{0.75}O_2$ is almost equal to that of pure ThO_2 implying an almost equal rate of oxygen diffusion in all cases. Table 2 shows migration and binding energies of an oxygen vacancy adjacent to Th^{4+} in NpO_2 and Np^{4+} in ThO_2. The binding energy (E_b) is negative in the case of Th^{4+} present as a dopant in NpO_2 signifying that the oxygen vacancy does not favor the 1st NN position with respect to the Th^{4+} dopant ion in NpO_2. Conversely, E_b is positive in the case of Np^{4+} present as dopant in ThO_2. The migration barrier for oxygen increases from 0.419 eV in defect free NpO_2 to 0.470 eV in the presence of single Th^{4+} at 1st NN to 0.583 eV when there are two Th^{4+} cations at 1st and 2nd NN site. This is consistent with the decrease in oxygen diffusion in NpO_2 as a function of ThO_2 concentration as shown in the MSD curve. The oxygen migration barrier decreases from 0.537 eV in defect free ThO_2 to 0.413 eV in the presence of a single Np^{4+} at 1st NN and 0.250 eV when Np^{4+} cations are present at 1st and 2nd NN sites. The lower migration barrier with increasing NpO_2 concentration is a consequence of the smaller ionic radius of Np^{4+} (0.98 Å) compared to Th^{4+} (1.05 Å) thereby providing more open space for oxygen ions to migrate. At a high concentration of NpO_2 (*i.e.* $Np_{0.25}Th_{0.75}O_2$) the lower oxygen diffusivity in ThO_2 is compensated by the higher oxygen diffusivity in NpO_2, resulting in a MSD slope almost identical to that of ThO_2. Aidya *et al.* calculated oxygen diffusivity in $(Th,Ce)O_2$ and $(Th,U)O_2$ MOX and found that with increasing Ce or U concentration in ThO2, oxygen diffusivity decreases due to the oxygen vacancy binding with Ce or U. Conversely, with increasing Th concentration in CeO_2 or UO_2 oxygen diffusivity decreases due to the increasing migration barrier, this is in agreement with our results.

Table 2: Oxygen vacancy migration energies (E_m) calculated using static nudged elastic band (NEB) technique and binding energies (E_b) in ThO_2 when Np is present as a dopant (and vice versa) and in UO_2 when Np is present as a dopant (and vice versa). The calculated E_m values for pure oxides (ThO_2, UO_2 and NpO_2) are also compared with previous *ab-initio* and MD calculated values. Further, E_m is predicted from Arrhenius plot (diffusivity versus 1/temperature plot) by calculating mean square deviations (MSD) at different temperatures (from 750 to 2000 K in the interval of 250 K). 1st NN and 2nd NN refers to the near neighbour positions of the oxygen vacancy with respect to the dopant cation, 1st & 2nd implies two dopant ions in adjacent cation sites. The values of binding energies (E_b) shown in parenthesis are calculated using DFT calculation.

System	E_m(eV) MD (this study) From Static NEB	E_m(eV) MD (this study) From MSD	E_m(eV) Ab-initio (previous study)	E_m(eV) MD (previous study)
UO_2	0.401	0.393	0.67-1.34	0.3-0.5, 0.391
ThO_2	0.537	0.525	1.97-2.16	0.52-0.79, 0.530
NpO_2	0.419	0.423	-	0.42

System	Binding Energy(E_b) in eV 1st NN 2nd NN		Migration Energy(E_m) in eV 1st NN 1st & 2nd NN	
ThO_2:Np	0.284(0.368)	0.000	0.413	0.250
NpO_2:Th	-0.236(-0.984)	0.020	0.470	0.583
UO_2:Np	0.111(0.468)	0.000	0.371	0.360
NpO_2:U	- 0.160(-0.066)	0.000	0.518	0.521

Fig.3(b) compares the MSDs of UO_2, NpO_2 and $U_{1-x}Np_xO_2$ MOX compositions. The slope of the MSD curve for $U_{0.875}Np_{0.125}O_2$ lies between those of UO_2 and NpO_2. The higher MSD slope for UO_2 can be attributed to the lower E_m in UO_2 as compared to that in NpO_2
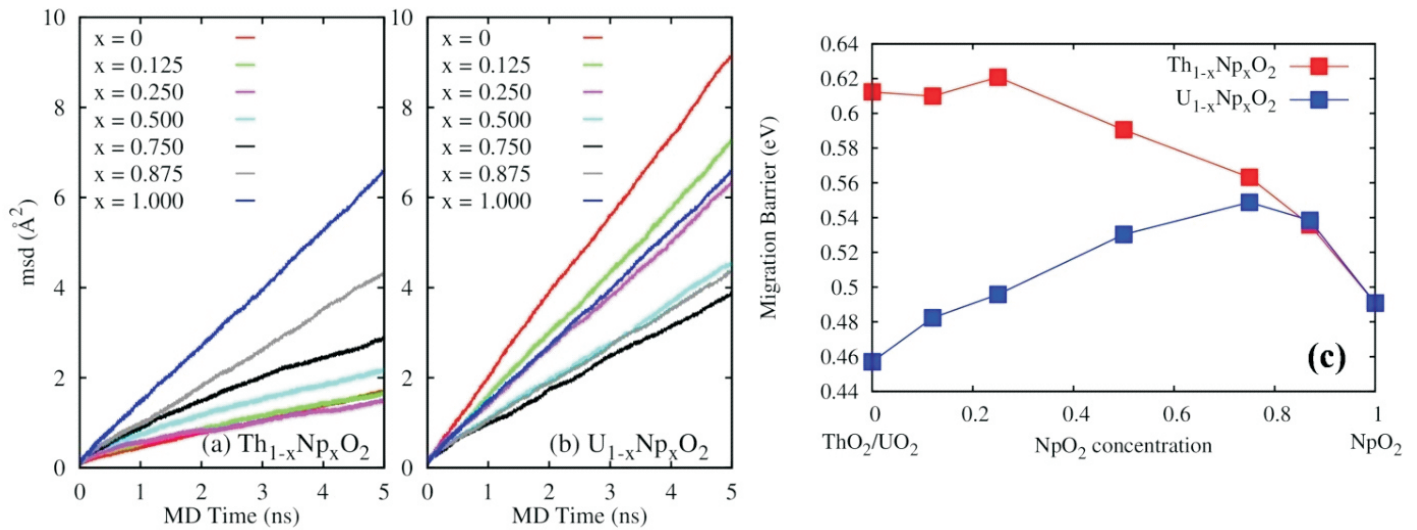
Fig.3: Mean square displacement (MSD) of oxygen as a function of MD simulation time in (a) $Th_{1-x}Np_xO_2$ and (b) $U_{1-x}Np_xO_2$ MOX calculated at 750 K. (c) The migration barriers (E_m) of oxygen vacancy in $Th_{1-x}Np_xO_2$ and $U_{1-x}Np_xO_2$ MOX as a function of NpO_2 concentration evaluated from MD calculated oxygen diffusivity as a function of temperature (Arrhenius plot).

(Table 2). With further increase of Np concentration, the slope of the MSD curve for $U_{0.75}Np_{0.25}O_2$ is almost equal to that of NpO_2. The slope of the MSD curves for other $U_{1-x}Np_xO_2$ MOX compositions are less than that of NpO_2. The migration barrier for the oxygen vacancy decreases from 0.401 eV in UO_2 to 0.371 eV in the presence of a single Np^{4+} ion at 1st NN to 0.360 eV in the presence of two Np^{4+} ions at 1st and 2nd NN. The lower migration barrier with increasing NpO_2 concentration is a consequence of the smaller ionic radius of Np^{4+} (0.98 Å) compared to U^{4+} (1.00 Å) thereby providing more open space for oxygen ions to migrate as discussed for $(Th,Np)O_2$ MOX. Moreover, the binding energy of the oxygen vacancy in UO_2 in the presence of Np as 1st NN is positive implying the oxygen vacancy prefers to stay as the 1st NN to the Np^{4+} dopant ion in UO_2. This leads to the continuous decrease of the MSD slope in $U_{1-x}Np_xO_2$ MOX going from UO_2 to NpO_2. The binding energy of the oxygen vacancy in NpO_2 in the presence of U^{4+} as 1st NN is negative. Also the migration barrier of oxygen via a vacancy mechanism increases from 0.419 eV in NpO_2 to 0.518 eV in the presence of single U^{4+} ion at 1st NN to 0.521 eV with U^{4+} present at 1st and 2nd NN sites. This is consistent with the MSD slope reducing with increasing UO_2 concentration.

In order to further assess oxygen diffusion properties of MOX the MSDs were calculated for 5 ns using a 10x10x10 supercell (containing 12000 atoms) for a temperature range from 750 K to 2000 K (in 250 K interval). Overall features of MSD curve describe at 750 K is valid for MSD curve at higher temperatures but spread in MSD value at the end of 5 ns reduces drastically at higher temperature. The rate of reduction is higher for $U_{1-x}Np_xO_2$ compared to $Th_{1-x}Np_xO_2$ MOX. The MSD is related with oxygen diffusivity (D) by the relation MSD = 6Dt, where t is the MD time and in this case t = 5 ns. By assuming Arrhenius relationship the D is related to the migration energy (E_m) as

$$D = D_0 \exp(E_m/k_BT) \qquad (5)$$

where D_0 is the pre-exponential term, k_B and T is Boltzman constant and temperature, respectively. From the logarithmic plot of D as a function of $1/T$, E_m is determined over the NpO_2 concentration in MOX and those values are shown in Figure 3(c). The E_m values of the oxides derived from the Arrhenius plot are also shown in Table 2 and those values are matching within 2.5% of E_m values determined

from static NEB calculations. Moreover the sequence of the E_m values of the oxides is consistent with that determined from NEB calculations. Fig.3(c) shows slight increase of E_m with increase of NpO_2 concentration for $Th_{1-x}NpO_2$ MOX up to x=0.25 followed by continuous decrease up to x=1.0. On the contrary, the E_m increases continuously with increasing NpO_2 concentration up to x=0.75 followed by decreasing trend up to x=1.0. Fig.3(c) clearly shows nonlinear variation of the E_m with NpO_2 concentration and maxima lies around x=0.25 and 0.75 for $Th_{1-x}NpO_2$ and $U_{1-x}NpO_2$ MOX, respectively.

Conclusions

Main conclusions of the present study are as follows:

a) The calculated ΔH_{mix} of $Th_{1-x}Np_xO_2$ MOX were positive compared to the end members and nearly symmetric around x=0.5 and ΔH_{mix} of AFM configuration is higher compared to FM configuration maximum by 0.19 kJ/mole. The ΔH_{mix} of $U_{1-x}Np_xO_2$ MOX were negative up to $U_{0.50}Np_{0.50}O_2$ with maximum value of -1.21 kJ/mole at $U_{0.4375}Np_{0.5625}O_2$ whereas Np-rich $(U,Np)O_2$ MOX compositions exhibited ΔH_{mix} close to zero. Value of ΔH_{mix} for $(Th,Np)O_2$ are consistent with a simple miscibility-gap phase diagram while those for $(U,Np)O_2$ suggest a more complex behaviour. Nevertheless, lattice parameters variation with compositions till follows a Vegard's law relationship.

b) The calculated lattice parameter versus temperature curves of UO_2, NpO_2 and $U_{0.875}Np_{0.125}O_2$ match well within 1% of high temperature XRD values. At higher compositions of NpO_2, our MD calculated values are over prediction of high temperature XRD values (within 2%) throughout the temperature range. Linear thermal expansion coefficients (LTEC) of $Th_{1-x}Np_xO_2$ increase with NpO_2 concentration; while LTEC of $U_{1-x}Np_xO_2$ decreases with NpO_2 concentration.

c) The degradation of thermal conductivity in $U_{1-x}Np_xO_2$ is far less significant compared to that in $Th_{1-x}Np_xO_2$. This is governed by the fact that Np has very similar ionic radius and atomic mass as that of U than Th and defect-phonon scattering is less in $U_{1-x}Np_xO_2$. Therefore, generation of 6.25 atom% of Np (as minor actinide) degrades the thermal-conductivity of ThO_2-base MOX fuel by 24.0-12.5 % in the 750-1000 K temperature range. Conversely, mixing of

Np with UO_2-based MOX fuel up to by 50 atom% degrades the thermal-conductivity only by 13-2.3% in the 750-1000 K temperature range.

d) The oxygen diffusivities in $Th_{1-x}Np_xO_2$ and $U_{1-x}Np_xO_2$ MOX are calculated and are found to be higher in UO_2 and NpO_2 compared to that in ThO_2 due to lower oxygen migration barriers. With the addition of Th^{4+} to NpO_2, the diffusivity decreases due to the increase in the migration barriers introduced by a larger ionic radius of Th^{4+} compared to Np^{4+}. However, addition of Np^{4+} to ThO_2 decreases oxygen diffusion due to oxygen vacancy binding with Np^{4+}, even though the migration barriers decrease due to the smaller size of Np^{4+} than the host Th^{4+}. Similar observation can be made in $U_{1-x}Np_xO_2$. Our MD calculated binding energies follow the trend in isolated oxygen Frenkel pair defect energies (O-FP$_{isolated}$) of individual actinide oxides. Moreover, our MD calculated oxygen vacancy binding energy is consistent with the DFT calculated binding energies.

e) A database of thermal expansion, thermal conductivity and oxygen diffusion parameters has been developed which can be used to design new generation fuels.

Corresponding Author*

A.K. Arya (aarya@barc.gov.in)

References

[1] Actinide and fission product partitioning and transmutation, Status and assessment Report, NEA, OECD, 1999.

[2] V. Anastasov, M. Betti, F. Boisson, F. Depisch, F. Houlbreque, R. Jeffree, I. Khamis, S. Lattemann, J. Miquel, S. Nisan, Status of minor actinide fuel development, IAEA nuclear energy series, 2009.

[3] R. Konings, J. Kloosterman, *Progress in Nuclear Energy,* 2001, **38**, 3, 331-334.

[4] P. Dey, M. Giroux, A. Khaperskaya, J. Laidler, A. Machiels, M. Masson, F. Storrer, G. Uchiyama, Spent fuel reprocessing options, IAEA-TECDOC-1587.

[5] V. Smirnov, V. Sobolev, J. Somers, R. Srivenkatesan, A. Stanculescu, V. Subbotin, A. Surenkov, T. Suzuki, M. Szieberth, S. Taczanowski, Advanced reactor technology options for utilization and transmutation of actinides in spent nuclear fuel, IAEA-TECDOC-1626.

[6] International Atomic Energy Agency, Thorium fuel cycle-potential benefits and challenges, IAEA-TECDOC-1450, IAEA, Vienna, 2005.

[7] P.S. Ghosh, P.S. Somayajulu, A. Arya, G.K. Dey and B.K. Dutta, *J. Alloys Compd.*, 2015, **638,** 172-181.

[8] P.S. Ghosh, P.S. Somayajulu, R. Krishnan, N. Pathak, A. Arya and G. K. Dey, *J. Alloys Compd.*, 2015, **650,** 165-177.

[9] P.S. Ghosh, N. Kuganathan, C.O.T. Galvin, A. Arya, G.K. Dey, B.K. Dutta and R.W. Grimes, *J. Nucl. Mater.*, 2016, **476,** 112-122.

[10] P.S. Ghosh, A. Arya, N. Kuganathan, G.K. Dey and R.W. Grimes, *Physical Chemistry Chemical Physics,* 2016, **18,** 31494-31504.

[11] P.S. Somayajulu, P.S. Ghosh, A. Arya, K.V. Vrinda Devi, D. B. Sathe, J. Banerjee, K. B. Khan, G.K. Dey and B.K. Dutta, *J. Alloys Compd.*, 2016, **664,** 291-303.

[12] P.S. Somayajulu, P.S. Ghosh, J. Banerjee, K.L.N.C. Babu, K.M. Danny, B.P. Mandal, T. Mahata, P. Sengupta, S.K. Sali and A. Arya, *J. Nucl. Mater.*, 2015, **467,** 644-659.

[13] P.S. Ghosh and A. Arya, *Physical Chemistry Chemical Physics,* 2020, **22,** 6406-6417.

[14] P.S. Ghosh and A. Arya, *Physical Chemistry Chemical Physics*, 2019, **21,** 16818-16829.

[15] N. Kuganathan, P.S. Ghosh, A. Arya and R.W. Grimes, *Journal of Nuclear Materials.* 2018, **507,** 288-296.

[16] P.S. Ghosh, A. Arya, N. Kuganathan and R.W. Grimes, *Journal of Nuclear Materials*, 2019, **521,** 89-98.

[17] P.S. Ghosh, A. Arya, N. Kuganathan and R.W. Grimes, *Physical Chemistry Chemical Physics*, 2018, **20,** 18707-18717.

[18] N. Kuganathan, P.S. Ghosh, C.O.T. Galvin, A.K. Arya, B.K. Dutta, G.K. Dey, R.W. *Grimes, Journal of Nuclear Materials*, 2017, **485,** 47-55.

[19] N. Kuganathan, P.S. Ghosh, C.O.T. Galvin, A.K. Arya, G.K. Dey, R.W. Grimes, *Journal of Nuclear Materials*, 2017, **495,** 192-201.